RAA 2017 Vol. **17** No. **4**, 35 (14pp) doi: 10.1088/1674–4527/17/4/35

http://www.raa-journal.org *http://iopscience.iop.org/raa*

***R**esearch in*
***A**stronomy and*
***A**strophysics*

Gas emission and dynamics in the infrared dark cloud G31.23+0.05

Xiao-Lan Liu, Jun-Jie Wang, Jin-Long Xu, and Chuan-Peng Zhang

National Astronomical Observatories, Chinese Academy of Sciences, Beijing 100012, China; *liuxiaolan@bao.ac.cn*
NAOC-TU Joint Center for Astrophysics, Lhasa 850000, China

Received 2016 September 14; accepted 2016 December 21

Abstract We performed a multiwavelength study towards the infrared dark cloud (IRDC) G31.23+0.05 with new CO observations from Purple Mountain Observatory and archival data (the GLIMPSE, MIPSGAL, HERSCHEL, ATLASGAL, BGPS and NVSS surveys). From these observations, we identified three IRDCs with systemic velocities of 108.36 ± 0.06 (cloud A), 104.22 ± 0.11 (cloud B) and $75.73 \pm 0.07\,\mathrm{km\,s^{-1}}$ (cloud C) in the line of sight towards IRDC G31.23. Analyses of the molecular and dust emission suggest that cloud A is a filamentary structure containing a young stellar object; clouds B and C both include a starless core. Clouds A and B are gravitationally bound and have a chance to form stars. In addition, the velocity information and the position-velocity diagram suggest that clouds A and B are adjacent in space and provide a clue hinting at a possible cloud-cloud collision. Additionally, the distribution of dust temperature shows a temperature bubble. The compact core in cloud A is associated with an UCHII region, an IRAS source, H_2O masers, CH_3OH masers and OH masers, suggesting that massive star formation is active there. We estimate the age of the HII region to be (0.03–0.09) Myr, indicating that the star inside is young.

Key words: stars: formation — ISM: HII regions — ISM: molecules — ISM: individual (IRDC G31.23+0.05) — ISM: kinematics and dynamics

1 INTRODUCTION

Infrared dark clouds (IRDCs) were discovered as dark silhouettes against the bright Galactic mid-infrared (MIR) background by the Infrared Space Observatory (ISO; Perault et al. 1996) and the Midcourse Space Experiment (MSX; Carey et al. 1998; Egan et al. 1998). Millimeter (mm)/submillimeter research suggests that the majority of IRDCs are filamentary, cold ($T < 25\,\mathrm{K}$), dense ($\sim 10^5\,\mathrm{cm^{-3}}$) and have high column density ($\geq 10^{22}\,\mathrm{cm^{-2}}$), with a scale of $1 \sim 10\,\mathrm{pc}$ and a mass range of $10^2 \sim 10^5\,M_\odot$. In addition, a number of them are associated with high-mass ($> 8\,M_\odot$) star formation (e.g. Rathborne et al. 2006; Busquet et al. 2013; Liu et al. 2013, 2014).

Previous observations indicated that IRDCs have complicated kinematics with numerous filamentary substructures (e.g. Sanhueza et al. 2013; Henshaw et al. 2013; Peretto et al. 2014; Jiménez-Serra et al. 2014; Henshaw et al. 2014; Pon et al. 2016). Henshaw et al. (2013) and Peretto et al. (2014) have found that IRDCs can contain multiple separate velocity components which are not obvious simply from the spatial information. These large-scale kinematic signatures provide important clues on the process of star formation and have the possibility of revealing the impact of colliding flows (e.g. Vázquez-Semadeni et al. 2009; Jiménez-Serra et al. 2010; Dobbs et al. 2014; Beuther et al. 2015), cloud-cloud collisions (e.g. Furukawa et al. 2009; Duarte-Cabral et al. 2011; Henshaw et al. 2013; Higuchi et al. 2014; Dirienzo et al. 2015) and global gravitational collapse (e.g. Ballesteros-Paredes et al. 2011) in producing the larger molecular clouds themselves as well as prestellar cores.

IRDC G31.23+0.05 was associated with an ultra-compact HII (UCHII) region G31.28+0.06, which was well studied at centimeter (cm) and mm wavebands (Kurtz et al. 1994; Becker et al. 1994; Bronfman et al. 1996; Mateen et al. 2006). The distance of UCHII region G31.28+0.06 was $4.27^{+0.87}_{-0.64}$ kpc by the method of

parallax measurement (Zhang et al. 2014). H_2O masers (Forster & Caswell 1989, 1999), OH masers (Forster & Caswell 1989, 1999; Szymczak & Gérard 2004; Caswell et al. 2013) and class II CH_3OH masers (Szymczak et al. 2000; Błaszkiewicz & Kus 2004) were detected and found to be associated with UCHII region G31.28+0.06, indicating that it is an active massive star formation region.

In this paper, we present the detections of widespread ^{13}CO (1–0) and C^{18}O (1–0) emission towards IRDC G31.23+0.05. Here, we mainly utilize C^{18}O (1–0) to trace the structure and kinematics in this region, together with ^{13}CO (1–0) for the star formation activities. With regard to the remaining parts of this paper, Section 2 gives a description about the data archive and Section 3 is about the results and analyses. A discussion is presented in Section 4. We summarize our conclusions in Section 5.

2 OBSERVATIONS AND DATA REDUCTION

2.1 Purple Mountain Observatory Data

The mapping observations of IRDC G31.23+0.05 were performed in the ^{13}CO (1–0) and C^{18}O (1–0) lines using the Purple Mountain Observatory (PMO) 13.7 m radio telescope at Delingha in the west of China at an altitude of 3200 meters, in May 2012. The new 9-beam array receiver system in single-sideband (SSB) mode was used as a front end. Fast Fourier transform spectrometers were used as a back end, which had a total bandwidth of 1 GHz and 16 384 channels, corresponding to a velocity resolution $\sim 0.17\,\mathrm{km\,s^{-1}}$ for ^{13}CO (1–0) and C^{18}O (1–0). The half-power beam width at observing frequencies 110.20 GHz (^{13}CO) and 109.78 GHz (C^{18}O)[1] was $\sim 50.1''$ [2]. The pointing accuracy of the telescope was better than $4''$. The system noise temperature ($T_{\rm sys}$) in the SSB mode varied between 150 K and 400 K. The root mean square noise level per channel was 0.22 K. The phase center of the observations was $\alpha(\mathrm{J2000}) = 18^{\rm h}48^{\rm m}09.32^{\rm s}$, $\delta(\mathrm{J2000}) = -01°29'30.6''$ with the position-switch On-the-Fly (OTF) mode, scanning a $20'$ by $20'$ region at a rate of $50''$ per second with a dump time of 0.3 s. However, the edges of the OTF maps were noisy and thus only the central $13' \times 13'$ region was selected for further analysis. The standard chopper wheel calibration technique was used to measure antenna temperature $T_{\rm A}^{\star}$ corrected for atmospheric absorption. The final data were recorded in a brightness temperature scale of $T_{\rm mb}$ (K). The correction for line intensities to the main beam brightness temperature scale was made using the formula $T_{\rm mb} = T_{\rm A}^{\star}/\eta_{\nu}$, where η_{ν} is the main beam efficiency of about 0.5. The data were reduced by the software Continuum and Line Analysis Single-Dish Software (CLASS) and Grenoble Graphic (GreG) [3]. We used the routine XY_MAP in CLASS to regrid raw data and then converted them into FITS files. The pixel size of these FITS files was $30'' \times 30''$.

2.2 Archival Data

The Spitzer IRAC 8 μm, MIPS 24 μm, Herschel PACS 70, 160 μm together with SPIRE 250, 350, 500 μm images, the ATLASGAL 870 μm and the 1.1 mm continuum data were obtained from the Galactic Legacy Infrared Mid-Plane Survey Extraordinaire (GLIMPSE), a 24 and 70 Micron Survey of the Inner Galactic Disk with MIPS (MIPSGAL)[4], the Herschel Science Archive (HSA)[5] (Poglitsch et al. 2010; Griffin et al. 2010), the ATLASGAL Database Server[6], and the Bolocam Galactic Plane Survey (BGPS)[7] (Glenn et al. 2009). The 1.4 GHz radio continuum emission data were obtained from the NRAO VLA Sky Survey (Condon et al. 1998).

The GRS C^{13}O (1–0) (Jackson et al. 2006) data have a full width at half maximum beam size of $\sim 46''$ on a $22''$ grid with a spectral resolution of $0.21\,\mathrm{km\,s^{-1}}$. Since this data set has better spatial resolution and a smaller grid, which means more observation points in the same region, it is more accurate to trace the C^{13}O distribution and the position-velocity (PV) diagram. However, the ^{13}CO (1–0) data of PMO are mainly utilized to calculate the physical parameters and provide spectral information.

3 RESULTS

3.1 CO and Continuum Emission of IRDC G31.23+0.05

Figure 1 shows the average spectra of ^{13}CO (1–0) and C^{18}O (1–0) lines over IRDC G31.23+0.05. Several components were detected in a range of (60–120) $\mathrm{km\,s^{-1}}$ (see Figs. 1 and A.1). In order to examine the velocity components associated with IRDC G31.23+0.05, we make the

[1] *http://www.astro.uni-koeln.de/cdms/entries*
[2] *http://english.dlh.pmo.cas.cn/fs/*
[3] *http://www.iram.fr/IRAMFR/GILDAS*
[4] *http://irsa.ipac.caltech.edu/data/SPITZER/GLIMPSE*
[5] *http://irsa.ipac.caltech.edu/applications/Herschel*
[6] *http://third.ucllnl.org/cgi-bin/gpscutout* (Schuller et al. 2009)
[7] *http://irsa.ipac.caltech.edu/data/BOLOCAM_GPS/*

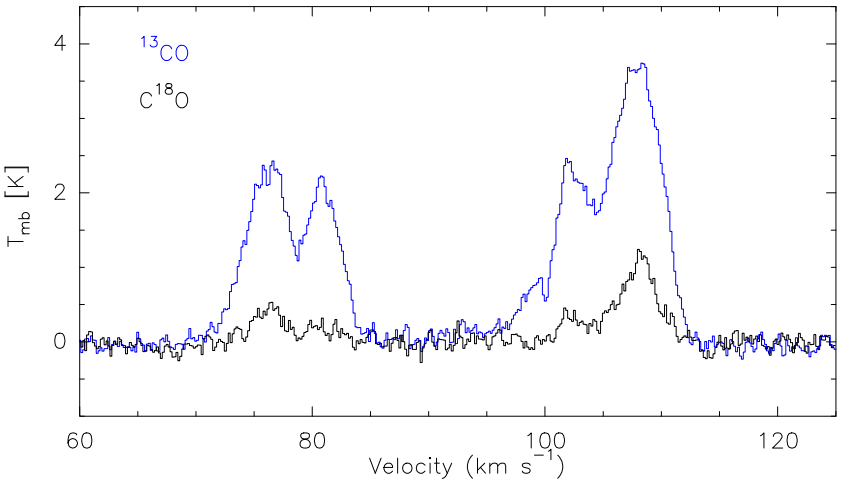

Fig. 1 The average spectra in ^{13}CO (1–0) and C^{18}O (1–0) lines which show several velocity components along the line of sight direction towards IRDC G31.23+0.05.

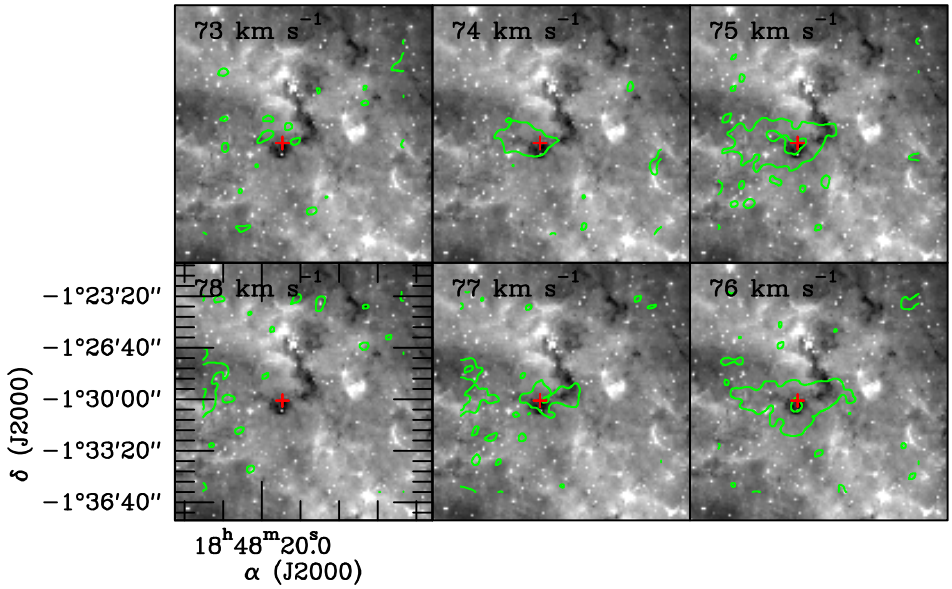

Fig. 2 Channel maps in the C^{18}O (1–0) line over the velocity interval of (73–79) km s^{-1}. The integrated velocity interval of each subfigure is 1 km s^{-1} and the value in the top-left is the start. The *green contour levels* start at 3σ in steps of 3σ ($\sigma = 0.15$ K km s^{-1}) and "+" symbols mark the peak positions of C^{18}O (1–0) emission in cloud C. Grey-scales display the Spitzer 8 μm continuum image of IRDC G31.23+0.05.

Table 1 Observed Parameters of Each Line

IRDCs	α	δ	Range	C^{18}O(1 − 0)				^{13}CO(1 − 0)			
				$T_{\rm mb}$	$\int T_{\rm mb}dV$	$V_{\rm LSR}$	ΔV	$T_{\rm mb}$	$\int T_{\rm mb}dV$	$V_{\rm LSR}$	ΔV
	(J2000.0)	(J2000.0)	(km s^{-1})	(K)	(K km s^{-1})	(km s^{-1})		(K)	(K km s^{-1})	(km s^{-1})	
(1)	(2)	(3)	(4)	(5)	(6)	(7)	(8)	(9)	(10)	(11)	(12)
A	18:48:11.281	–01:26:40.26	(105.00–112.71)	2.87(0.27)	14.39(0.37)	108.36(0.06)	4.85(0.15)	9.15(0.27)	47.29(0.34)	108.29(0.17)	4.85(0.17)
B	18:48:07.685	–01:26:25.55	(101.04–106.67)	1.88(0.32)	8.12(0.44)	104.22(0.11)	4.04(0.26)	5.67(0.30)	26.72(1.14)	103.74(0.09)	4.43(0.18)
C	18:48:14.664	–01:30:03.59	(73.09–77.78)	1.50(0.23)	4.16(0.23)	75.73(0.07)	2.61(0.17)	4.50(0.22)	18.39(0.28)	75.64(0.03)	3.84(0.07)

Notes: Columns are (1) cloud name, (2)–(3) right ascension and declination of the peak positions respectively, (4) velocity ranges associated with the clouds, (5)–(8) Gaussian fitting parameters of the C^{18}O (1–0) lines, (9)–(12) Gaussian fitting parameters of the ^{13}CO (1–0) lines.

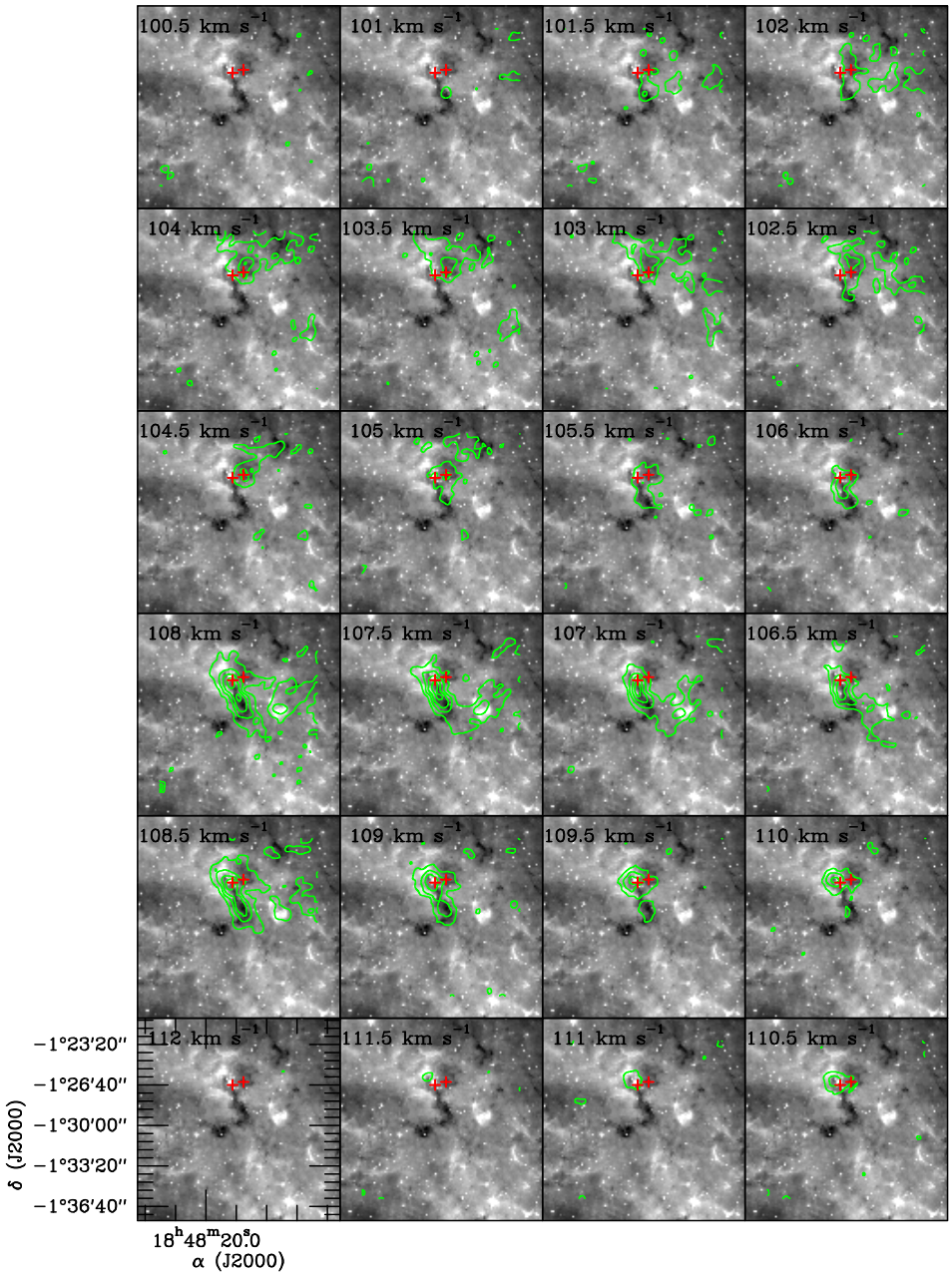

Fig. 3 The channel maps in the $C^{18}O$ (1–0) line over the velocity interval of (100.5–112.5) km s^{-1}. The integrated velocity interval of each subfigure is 0.5 km s^{-1} and the value in the top-left is the start. The *green contour levels* start at 3σ in steps of 3σ ($\sigma = 0.12$ K km s^{-1}) and "+" symbols mark the peak positions of $C^{18}O$ (1–0) emission in both clouds A and B. Grey-scales display the Spitzer 8 μm continuum image of IRDC G31.23+0.05.

channel maps of $C^{18}O$ (1–0) over the above velocity interval and detect three different velocity components associated with three separate extinction dark silhouettes, as shown in Figures 2 and 3. It is likely that three independent IRDCs are identified in these observations. We have denoted their peak positions of the $C^{18}O$ (1–0) emission with "+" symbols in Figures 2 and 3. For distinction, we name these clouds "A," "B" and "C." In order to determine the systemic velocity and velocity coverage of each cloud, we extract spectra from the peak position of each component and fit Gaussians (see Fig. 4).

The fitting parameters are summarized in Table 1. The velocity ranges of the three components are (73.09–77.78), (101.04–106.67) and (105.00–112.71) km,s^{-1} with centroid velocities of 108.36 ± 0.06 (cloud A), 104.22 ± 0.11 (cloud B) and 75.73 ± 0.07

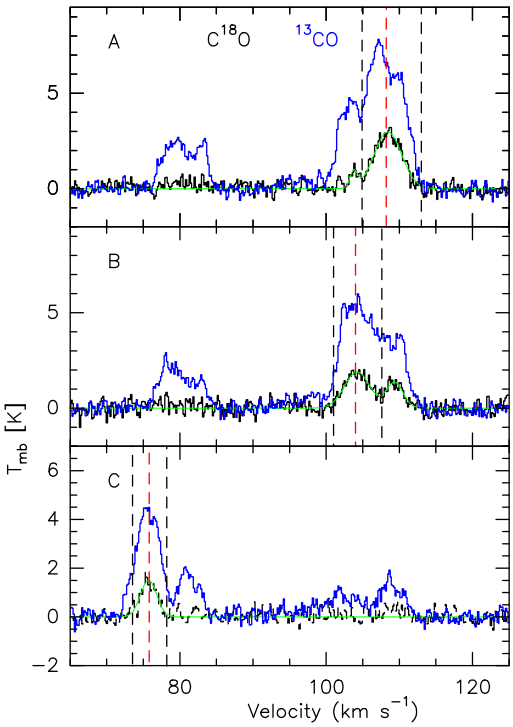

Fig. 4 Extracted spectra from the peak positions of $C^{18}O$ (1–0) emission in clouds A, B and C in the molecular lines ^{13}CO (*blue*) (PMO) and $C^{18}O$ (*black*). The *green lines* are Gaussian fits to the $C^{18}O$ (1–0) lines. The *red dashed lines* in each panel mark the centroid velocity of each cloud and the *black dashed lines* in each subfigure denote the velocity range associated with each IRDC. The name of the corresponding cloud for every panel is shown in the top-left corner.

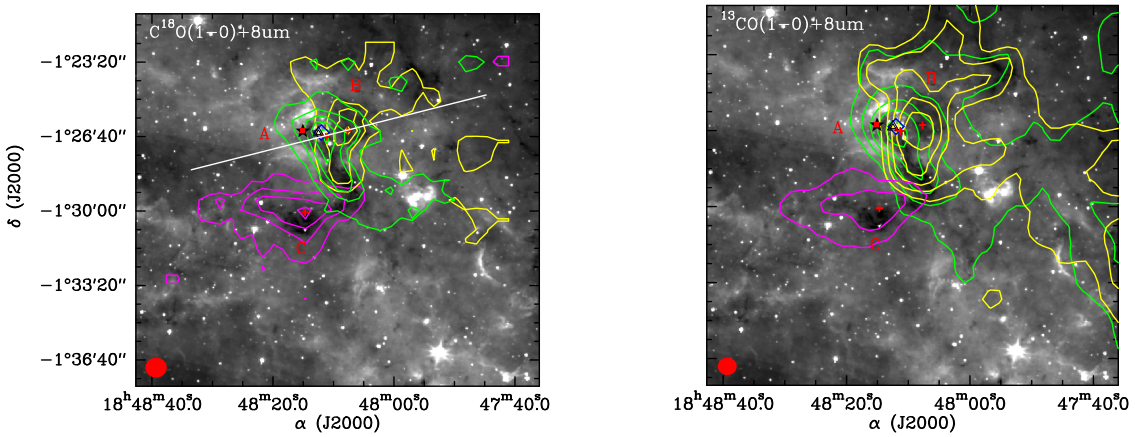

Fig. 5 Integrated intensity maps in $C^{18}O$ (1–0) (*left*) and GRS ^{13}CO (1–0) (*right*) lines of three clouds superposed on the Spitzer 8 μm emission. The integrated velocity intervals of clouds A, B and C are $(105.00 - 112.71)$ km s^{-1}, $(101.04 - 106.67)$ km s^{-1} and $(73.09 - 77.78)$ km s^{-1}, respectively. *Left*: The *green contour levels* start at 5σ in steps of 5σ for cloud A, the *yellow contour levels* start at 5σ in steps of 5σ for cloud B and the *magenta contour levels* start at 3σ in steps of 2σ for cloud C ($\sigma = 0.5$ K km s^{-1}); *Right*: The *green contour levels* start at 3σ in steps of 2σ for cloud A, the *yellow contour levels* start at 3σ in steps of 1σ for cloud B and the *magenta contour levels* start at 3σ in steps of 1σ for cloud C ($\sigma = 1.84$ K km s^{-1}). The beam size of each subfigure is indicated at the bottom-left corner. The symbols "◇," "△," "⋆," "■," "▲," "+" and letters (A, B and C) denote the location of an UCHII region, OH masers, IRAS 18456-0129, CH_3OH masers, H_2O masers, the peak positions and name of clouds, respectively. The *straight line* shows the cutting direction of the PV diagram in Figure 8.

(cloud C) $\mathrm{km\,s^{-1}}$, respectively. There is an additional component seen in the ^{13}CO at (79–85) $\mathrm{km\,s^{-1}}$, but it seems not spatially associated with any of the infrared dark regions. We will not discuss it.

Based on the above velocity ranges, we make the integrated intensity maps of clouds A, B and C, shown in Figure 5. The green contours represent cloud A, the yellow contours are for cloud B and the magenta contours are for cloud C.

In Figure 5, the ^{13}CO (1–0) and C^{18}O (1–0) emissions show similar morphologies. However the ^{13}CO (1–0) emission is more extended. Both the 8 μm and C^{18}O (1–0) emissions of cloud A show a northeast to southwest filament structure with a compact core located in its north portion. Additionally, the center of the compact core coincides with the peak position of the C^{18}O (1–0) emission in cloud A, and is associated with the UCHII G31.28+0.06 (♢), IRAS 18456–0129 (⋆), H_2O masers (▲), OH masers (△) and CH_3OH masers (■), implying potentially massive star formation. Cloud B displays an elongated north to south single-core structure and conversely cloud C is an east to west clump including a core in the west part in the C^{18}O (1–0) emission. Clouds A, B and C in Figure 5 overlap partly with each other in projection.

Figure 6 presents multiwavelength observations towards IRDC G31.23+0.05 from 8 μm to 1.1 mm. The 8 μm emission mainly originates from polycyclic aromatic hydrocarbons (PAHs; Watson et al. 2008), which are excited in the photodissociation region by ultraviolet radiation within the HII region (Pomarès et al. 2009). The 24 and 70 μm emissions are mostly produced by relatively hot dust (≥ 40 K) (Faimali et al. 2012; Zhang et al. 2016). The 160, 250, 350 and 500 μm emissions are attributed to cool dust (15–25 K; Anderson et al. 2012). The 870 μm and 1.1 mm emissions are dominated by cold dust. From the 8 μm emission in Figure 6, three different extinction dark silhouettes are clearly presented. They are clouds A, B and C. The "+" symbols in Figure 6 mark the peak positions of each C^{18}O molecular cloud. The dust emission suggests that cloud A has two dust components: a compact core with a probable embedded young stellar object (YSO) (Chambers et al. 2009) and an extended tail shown at 160 μm to 1.1 mm emission, resembling the C^{18}O (1–0) emission and supporting the fact that C^{18}O (1–0) in cloud A is optically thin and can be utilized to investigate the structure and velocity information. In addition, an interesting thing can be discovered in the 160 μm to 1.1 mm images. A bulge is apparent in the northwest part of the compact core of cloud A, but is dark at 8 to 70 μm. This bulge coincides with cloud B. Both suggest that this bulge is a dust component associated with cloud B, not a part of cloud A. Obviously, clouds A and B are closely adjacent in space in terms of dust emission.

3.2 Physical Parameters Derived From the Herschel Data and Molecular Lines

Herschel observations covering a wide spread of wavelength (70–500 μm) can be utilized to investigate dust properties of the entire clouds. To do this, we perform the SED fitting pixel by pixel to obtain the distribution of dust temperature $T_{\rm dust}$ and H_2 column density $N_{\rm H_2}$ with four Herschel bands, 160, 250, 350 and 500 μm. The reason that 70 μm is excluded is that the 70 μm emission traces hotter components such as very small grains and warmer material heated by protostars. From Figure 6, only the compact core in cloud A shows bright 8, 24 and 70 μm emissions, which are mainly attributed to the forming massive star. On the whole, clouds A, B and C are dark at 70 μm. The four images were convolved to the same resolution of $43.8''$ and rebinned to the same pixel size of $11.5''$. Under the assumption of optically thin dust emission, a modified blackbody function for a single temperature can be expressed as

$$I_\nu = \kappa_{\nu 0}(\nu/\nu_0)^\beta B_\nu(T_{\rm d})\mu m_{\rm H} N_{\rm H_2}, \qquad (1)$$

where I_ν is the surface brightness; $B_\nu(T_{\rm d})$ is the blackbody function for the dust temperature $T_{\rm d}$; μ is the mean molecular weight and set to 2.8 (Kauffmann et al. 2008); and $m_{\rm H}$ is the mass of a hydrogen atom. The dust opacity per unit mass of both dust and gas is defined as $\kappa_\nu = \kappa_{\nu 0}(\nu/\nu_0)^\beta$, in which $\kappa_{\nu 0}$ is assumed to be $0.1\,\mathrm{cm^2\,g^{-1}}$ at 1 THz (Beckwith et al. 1990) under a gas-to-dust mass ratio of 100, and β is fixed to 2, a statistical value found in a large sample of HII regions (Anderson et al. 2012).

Setting $T_{\rm dust}$ and $N_{\rm H_2}$ as free parameters, the SED fitting was performed using the IDL program MPFITFUN[8] (Markwardt 2009). According to the analysis of Pitann et al. (2013), the uncertainties of temperatures and column densities are mainly from the underlying dust opacity model. The uncertainties resulting from local background fluxes in the IRDCs are smaller and negligible relative to those introduced by the calibration, data reduction and dust opacity models. Overall temper-

[8] *https://www.physics.wisc.edu/∼craigm/idl/fitting.html*

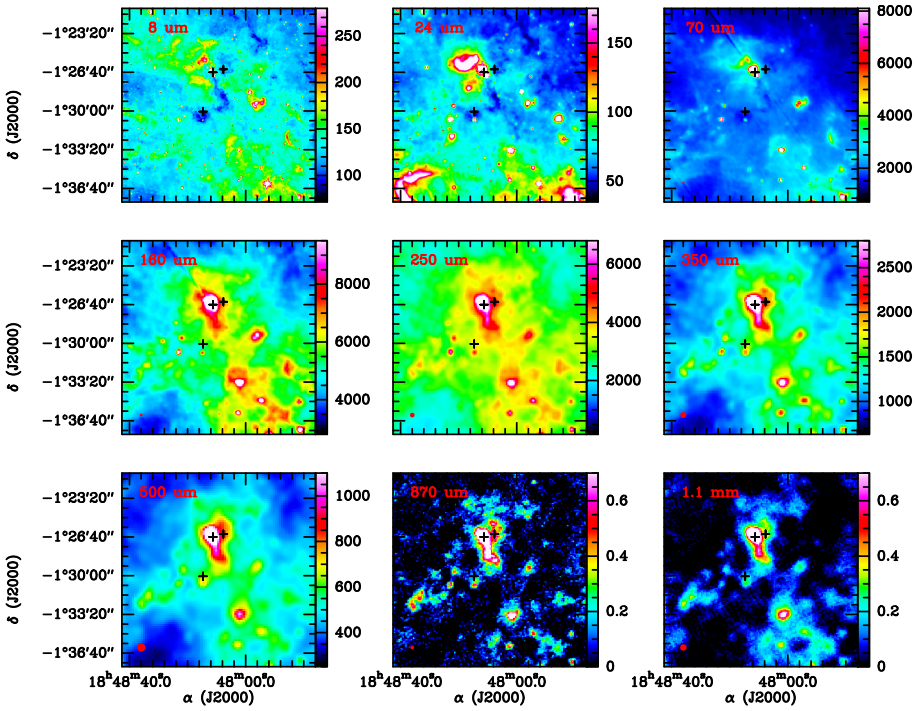

Fig. 6 Multiwavelength images of IRDC G31.3+0.05 from 8 μm to 1.1 mm. The beam of each panel is $1.9''$, $6.0''$, $10.7''$, $13.9''$, $23.9''$, $31.3''$, $43.8''$, $19.2''$ and $33.0''$. Each color bar indicates the flux with units Jy beam^{-1} for 8, 24, 70, 160, 250, 350, 500 and 870 μm to 1.1 mm, respectively. The "+" symbols represent the peak positions of $C^{18}O$ emission in clouds A, B and C.

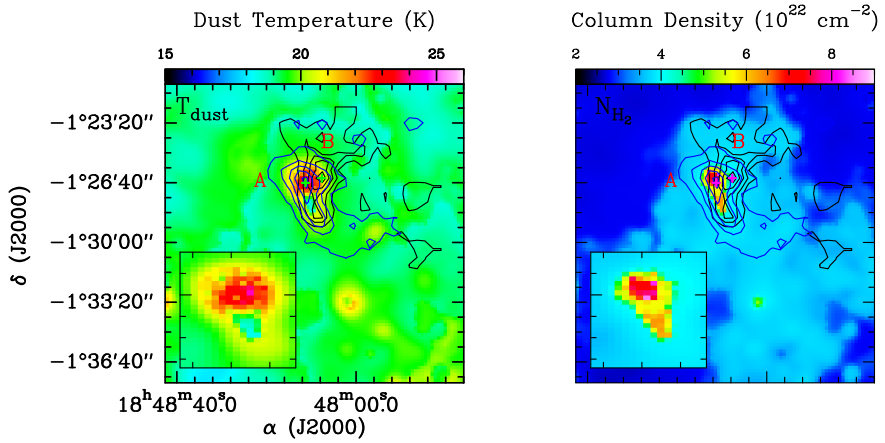

Fig. 7 Maps of the dust temperature $T_{\rm dust}$ and the H_2 column density $N_{\rm H_2}$ of IRDC G31.23+0.05. The two maps were constructed with the SED fitting pixel by pixel, centered at $\alpha = 18^{\rm h}48^{\rm m}09.32^{\rm s}$, $\delta = -01°29'30.6''$ J=2000.0. The "+" symbols and letters (A and B) signify the peak positions and the clouds, respectively. The zoomed-in subfigure in the bottom-left corner of each panel shows the temperature bubble region.

ature and column density uncertainties are assumed to be ± 1 K and 10%, respectively.

The resulting $T_{\rm dust}$ and $N_{\rm H_2}$ maps are presented in Figure 7. The blue and black contours represent integrated intensity maps of $C^{18}O$ (1–0) in clouds A and B, respectively. For the $T_{\rm dust}$ distribution in the left panel of Figure 7, the temperature has a range of $(16.9 - 24.7)$ K, with a maximum in the peak position of cloud A. This may be correlated with an embedded young protostar. Additionally, we find a temperature bubble (see the subfigure in the bottom-left corner in the left panel of Fig. 7) corresponding to a ~ 21 K shell surrounding the highest

temperature core at ~ 24 K and a cold cavity at ~ 18 K. The reason that this appears as a bubble may be due to protostar activity towards the peak of cloud A and the bubble may simply correspond to the edge of the core. While for the H_2 column density distribution in the right panel of Figure 7, the column density has an order of 10^{22} on the whole, with a maximum of 8.9×10^{22} cm^{-2} in the peak position of cloud A. Inside the temperature bubble, $N_{\rm H_2}$ shows an anti-correlation with $T_{\rm dust}$, except for the massive star formation region.

Additionally, through data provided by the molecular lines, we calculate the physical parameters $T_{\rm ex}$, $N_{\rm H_2}$, $n({\rm H_2})$, $M_{\rm LTE}$ and $M_{\rm vir}$ of clouds A and B using a trigonometric parallax measurement distance of $4.27^{+0.87}_{-0.64}$ kpc (Zhang et al. 2014), instead of the kinematic distance, since trigonometric parallax is the most reliable and assumption free method for astronomical distance measurement. However, the kinematic distances often have $> 20\%$ uncertainties, and they are highly dependent on location in the Galaxy (Reid et al. 2009). Here we assume cloud B has the same distance as cloud A due to the analysis in Section 4.1: clouds A and B may be adjacent in space. But for cloud C, we have no way to obtain a trigonometric parallax measurement distance and we use the kinematic distance of 4.10 ± 0.36 kpc. Under the assumption that C^{18}O (1–0) is optically thin, we can derive the optical depths of ^{13}CO and C^{18}O lines with the following equations from Myers et al. (1983)

$$\begin{aligned} &\frac{T_{\rm mb}(^{13}{\rm CO})}{T_{\rm mb}({\rm C^{18}O})} \simeq \frac{1-\exp(-\tau_{_{^{13}{\rm CO}}})}{1-\exp(-\tau_{_{\rm C^{18}O}})}, \\ &\frac{\tau_{_{^{13}{\rm CO}}}}{\tau_{_{\rm C^{18}O}}} = \frac{[^{13}{\rm CO}]}{[{\rm C^{18}O}]} \approx 5.5. \end{aligned} \tag{2}$$

The calculated optical depths of the ^{13}CO (1–0) and C^{18}O (1–0) lines in the peak positions of three clouds are listed in Table 2, Columns (3) and (4). We see that the ^{13}CO (1–0) line is optically thick and C^{18}O (1–0) is truly optically thin and hence the hypothesis is valid, so the excitation temperature $T_{\rm ex}$ of the clouds can be worked out by Equation (3).

$$T_{\rm ex} = \frac{5.29}{\ln[1+5.29/(T_{\rm mb}(^{13}{\rm CO})+0.89)]}. \tag{3}$$

The C^{18}O column density can be derived from the following formula (Scoville et al. 1986)

$$\begin{aligned} \frac{N({\rm C^{18}O})}{\rm cm^{-2}} =& 4.77\times10^{13} \times \frac{T_{\rm ex}+0.88}{\exp(-5.27/T_{\rm ex})} \\ &\times \frac{\tau}{1-\exp(-\tau)} \times \frac{\int T_{\rm mb} dv}{\rm K\ km\ s^{-1}}. \end{aligned} \tag{4}$$

As for the following analysis, we assume that the clouds are spherical and identified within the 5σ contours of the integrated intensity distribution. The characteristic size R means the radii of the cores, which are defined as $R = \sum r_i/i$, where r_i are the sizes of the cloud in different directions. The final results are listed in Column (5) of Table 2.

Taking the element abundance ratios

$$N({\rm H_2})/N(^{13}{\rm CO}) = 5\times10^5$$

and

$$N({\rm H_2})/N({\rm C^{18}O}) = 6\times10^6$$

(Frerking et al. 1982) and combining the above characteristic size, the derived mean volume densities of the H_2 molecule are

$$n({\rm H_2}) = N({\rm H_2})/2R. \tag{5}$$

Based on the assumption of local thermodynamic equilibrium (LTE) and spherical geometry, the masses of the clouds are calculated as

$$M_{\rm LTE} = \mu m_{\rm H} n({\rm H_2}) \times \Big(\frac{4}{3}\pi R^3\Big), \tag{6}$$

where $m_{\rm H}$ is the mass of a hydrogen atom and $\mu = 2.8$ is the mean molecular weight considering the contributions of He and other heavy elements to the total mass.

In addition, virial masses of the cores are also calculated by using Equation (7) under the assumption that the clouds have spherical geometry and the effect of magnetic fields is excluded,

$$M_{\rm vir} = 5(\Delta V)^2 R/(8\ln 2 \times G), \tag{7}$$

in which G is the gravitational constant. ΔV is the full width at half maximum of C^{18}O (1–0), which is displayed in Table 1, derived from the Gaussian fit. The uncertainties of the calculated virial masses are mainly produced by ΔV and R.

All the results are shown in Table 2. From Table 2, we can see that the excitation temperature $T_{\rm ex}$ 7–13 K is less than the dust temperature of $(16-25)$ K, but the average column densities $N_{\rm H_2}$ of clouds A, B and C have the same order as those derived from the Herschel data and that of Parsons et al. (2009). Hence, the assumptions for the calculation are feasible. The sizes of the clouds are in a range of $(2-4)$ pc, total masses are within a scope of $(0.8-6.0)\times10^4\,M_\odot$ and the mean $n({\rm H_2})$ has an order of 10^3 cm^{-3}. The derived physical parameters are similar to the previous studies for IRDCs (e.g. Rathborne et al. 2006; Busquet et al. 2013; Liu et al. 2013, 2014). In

addition, there is $M_{\rm LTE} \geqslant M_{\rm vir}$ for clouds A and B, indicating that they may be gravitationally bound and have a chance to collapse and form stars. while cloud C has $M_{\rm LTE} < M_{\rm vir}$, indicating that it may be gravitationally unbound.

4 DISCUSSION

4.1 A Collision between Clouds A and B?

In the velocity interval of (100–125) $\rm km\,s^{-1}$, the averaged spectra show double-peaked profiles in the $C^{18}O$ (1–0) and ^{13}CO (1–0). Together with the channel maps of $C^{18}O$ (1–0), we speculate that the two peak components indicate two clouds, named clouds A and B. Previously, some authors used a PV diagram to identify a cloud-cloud collision (Haworth et al. 2015; Dewangan et al. 2016). In order to verify whether cloud A is colliding with cloud B, we constructed the GRS ^{13}CO (1–0) PV diagram (Fig. 8) for the cut defined in Figure 5. From Figure 8, we find "a broad bridge feature," which connects two intensity peaks separated by lower intensity intermediate velocity emission, similar to the $10\,\rm km\,s^{-1}$ collision model in the middle panel of figure 5 of Haworth et al. (2015). The identified broad bridge is strong evidence of cloud-cloud collisions (Haworth et al. 2015; Dewangan et al. 2016).

Furthermore, Figure 9 shows the velocity structure (moment 1) and the velocity dispersion (moment 2) maps of $C^{18}O$ (1–0) for clouds A and B, respectively. The analyses of two clouds are performed over their respective velocity integrated range and above the integrated intensity 3σ ($\sigma = 0.5\,\rm K\,km\,s^{-1}$). Both clouds have non-uniform velocity and turbulence fields. Clouds A and B share a velocity component of (105.5–106.3) $\rm km\,s^{-1}$ at their overlapping region, inferred to be the broad bridge present in the PV diagram. In a cloud-cloud collision, gas at the impacting sites is expected to be more turbulent than at the non-impacting sites (Vallee 1995). In our observation, we can see that the star formation region in cloud A has line width broader than $2.2\,\rm km\,s^{-1}$ and the central region of cloud B has an enhanced line width of $\sim 1.8\,\rm km\,s^{-1}$. This can be explained by potential star formation activity or elevated temperature. Moreover, we find a different result from the studies of others (Vallee 1995; Sun & Wu 2013) in that both clouds A and B do not show enhanced turbulence ($\sim 1.8\,\rm km\,s^{-1}$ for cloud A and $< 1.0\,\rm km\,s^{-1}$ for cloud B) at the overlapping region. This seems to not support the scenario of cloud-cloud collision. Based on the above analyses, it appears difficult for us to judge whether the clouds are currently colliding each other. We will try to detect possible shock gas in future work.

4.2 Massive Star Formation in Cloud A

From the $C^{18}O$ (1–0) and ^{13}CO (1–0) emission, cloud A appears as a filament with a compact core included in its northeast part and an extended tail toward the southwest. Cloud B displays a single core structure and its south part seems to coincide with cloud A. The ^{13}CO (1–0) emissions are more diffuse than those of $C^{18}O$ (1–0) in clouds A and B. Meanwhile, the similar filamentary structure of cloud A also is traced by the continuum dust emission from 8 μm to 1.1 mm. This indicates that the $C^{18}O$ (1–0) emission is associated with the dust emission in cloud A. A compact core in cloud A shows strong emission at the MIR to mm band, suggesting that a YSO is embedded within it. At the location of cloud B, a north-to-south elongated structure is detected at 160 μm to 1.1 mm that is closely adjacent to cloud A. This suggests that cloud B is starless and may be adjacent to cloud A in space.

Figure 10 presents a comparison of the NVSS 1.4 GHz continuum with the $C^{18}O$ (1–0) emission of clouds A and B. The various symbols mark the locations of UCHII region G31.28+0.06, IRAS 18456–0129, OH masers, H_2O masers and CH_3OH masers, the information of which is summarized in Table 3. The NVSS 1.4 GHz radio emission can be used to trace the structure of the HII region, which shows a compact clump with a bulge towards the northeast in the compact core of cloud A. This indicates that the HII region is expanding and extending faster and farther in the northeast, which suggests that the ambient material is more diffuse in the northeast of cloud A. Actually, a dense region was found in the southwest part of the HII region (see the subfigure in the bottom-left corner in the right panel of Fig. 7) and has not yet been destroyed by radiation from the HII region.

In a quantitative way, we estimate the expanding dynamical age of this HII region by the model of Dyson & Williams (1980)

$$t_{\rm HII} = 7.2\times10^{4}\Big(\frac{R_{\rm HII}}{\rm pc}\Big)^{4/3}\times\Big(\frac{Q_{\rm Ly}}{10^{49}\,\rm ph\,s^{-1}}\Big)^{-1/4} \times\Big(\frac{n_{\rm i}}{10^{3}\rm cm^{-3}}\Big)^{-1/2}\,\rm yr\,, \quad (8)$$

where $R_{\rm HII}$ is the radius of the HII region, $n_{\rm i}$ is the initial number density of the gas and $Q_{\rm Ly}$ is the ionizing

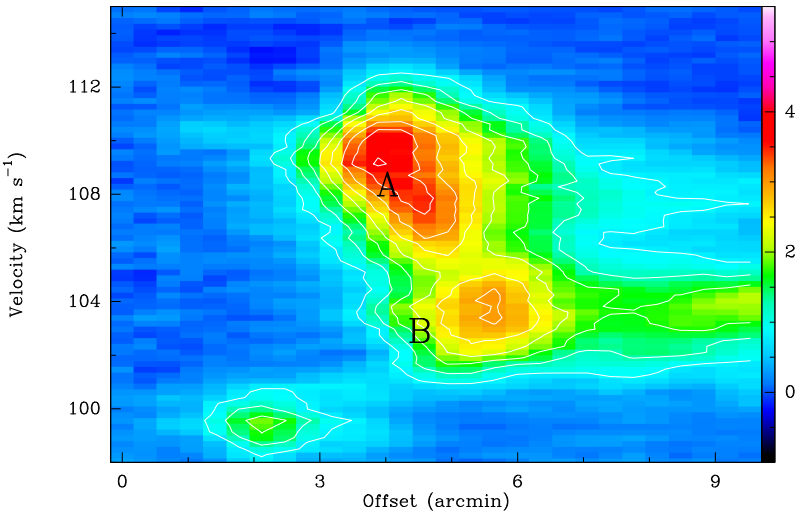

Fig. 8 PV diagram in GRS ^{13}CO (1–0) along the cutting path in Fig. 5. Letters (A and B) denote the velocity components corresponding to clouds A and B. The contour levels start at 3σ in steps of 1.5σ ($\sigma = 0.28$ K). The color bar represents the intensity with the unit K.

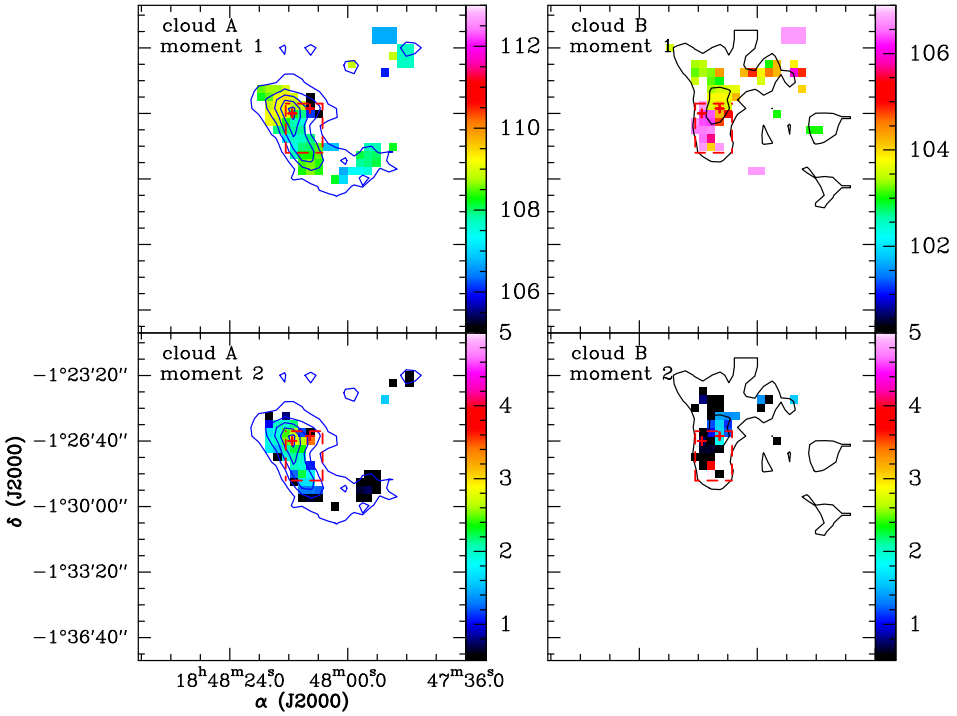

Fig. 9 Maps of C^{18}O (1–0) intensity-weighted mean velocity (*top*) and velocity dispersion (*bottom*) for clouds A and B. The units are in km s^{-1}. The moment maps for two clouds were performed over their respective integrated velocity range and above the integrated intensity 3σ ($\sigma = 0.5$ K km s^{-1}). The overlaid contours are the corresponding C^{18}O (1–0) integrated intensity maps of clouds A and B. The *red dashed rectangles* indicate the overlapping region of clouds A and B in each panel.

luminosity. The $R_{\rm HII}$ is about 0.40 pc from the NVSS 1.4 GHz emission above 3σ in Figure 10. Referring to the investigation of Longmore et al. (2007) towards this HII region, we can obtain the values of $n_{\rm i}$ and $Q_{\rm Ly}$ to be 4.3×10^2 cm^{-3} and 2.4×10^{47} ph s^{-1} respectively. Consequently, we derive the age of this HII region to be about 9.0×10^4 yr.

On the other hand, there is another way to estimate the lower limit on the age of the HII region. That is the sound crossing time $R_{\rm HII}/V_{\rm s}$, where $R_{\rm HII}$ is the size of the HII region and $V_{\rm s}$ is the sound velocity of

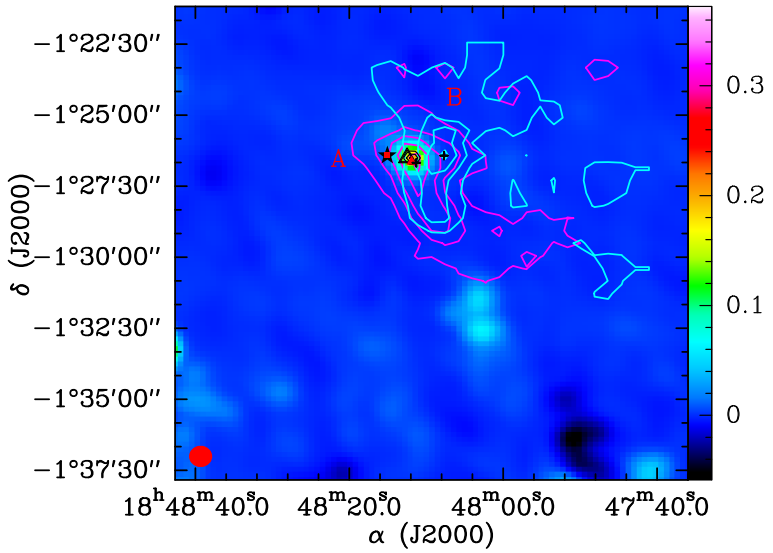

Fig. 10 Image of NVSS 1.4 GHz image + the *black contours* overlaid by the $C^{18}O$ (1–0) molecular emission ($K\,km\,s^{-1}$) of clouds A (the *magenta contours*) and B (the *aqua contours*). The *black contour levels* start at 3σ in steps of 1σ ($\sigma = 0.05\,Jy\,beam^{-1}$). The unit of each color bar is $Jy\,beam^{-1}$. The various symbols represent IRAS 18456–0129, OH masers, H_2O masers, CH_3OH masers and the core center, which are described in Table 3. The symbols "◇," "△," "⋆," "■," "▲," "+" and letters (A and B) denote the locations of an UCHII region, OH masers, IRAS 18456–0129, CH_3OH masers, H_2O masers, the peak positions and the clouds, respectively. The beam size is indicated at the bottom-left corner.

Table 2 The Physical Parameters Derived from the Molecular Lines

Cloud	T_{ex} (K)	$\tau_{C^{18}O}$	$\tau_{^{13}CO}$	R (pc)	$N(H_2)$ (10^{22} cm^{-2})	$n(H_2)$ (10^3 cm^{-3})	M_{LTE} ($10^4\,M_\odot$)	M_{vir} ($10^4\,M_\odot$)
(1)	(2)	(3)	(4)	(5)	(6)	(7)	(8)	(9)
A	12.5(0.3)	0.28(0.02)	1.54(0.11)	3.65(0.66)	9.6(0.4)	4.3(0.8)	6.0(3.4)	1.8(0.3)
B	8.9(0.3)	0.32(0.05)	1.76(0.28)	3.06(0.56)	4.8(0.4)	2.6(0.5)	2.1(1.2)	1.0(0.2)
C	7.7(0.2)	0.33(0.04)	1.82(0.22)	2.74(0.24)	2.4(0.2)	1.4(0.1)	0.8(0.2)	0.4(0.06)

the ionized gas. V_s can be estimated by the expression $V_s = \sqrt{2kT/m_{gas}}$. Here k is the Boltzmann constant, T is the temperature of ionized gas and m_{gas} is the mass of the ionized gas. The sound speed in the HII region is about $15\,km\,s^{-1}$ under the assumption $T \sim 10\,000$ K. Therefore, the sound crossing time is about $0.4\,pc/15\,km\,s^{-1} \approx 2.6 \times 10^4$ yr. Hence, the age of HII G31.28+0.06 is in the range $(0.03 - 0.09)$ Myr.

5 SUMMARY

Utilizing observations of ^{13}CO (1–0) and $C^{18}O$ (1–0) lines of the PMO 13.7 m radio telescope and auxiliary archival data involving seven public surveys (GRS, GLIMPSE, MIPSGAL, HERSCHEL, ATLASGAL, BGPS and NVSS), we investigated an infrared dark cloud G31.23+0.05 in detail. The main results are summarized below:

– We found that IRDC G31.23+0.05 consists of three relatively independent clouds A, B and C. Clouds A, B and C have systemic velocities of 108.36 ± 0.06, 104.22 ± 0.11 and $75.73 \pm 0.07\,km\,s^{-1}$, respectively. Cloud A is a filament with a compact core and an extended tail. Cloud B contains a north-to-south elongated core and cloud C has an east-to-west core included.
– The dust emission from 8 μm to 1.1 mm towards IRDC G31.23+0.05 also shows three independent IRDCs with similar dust structures to those of the molecular lines. The compact core of cloud A presents strong emission at 8, 24 and 70 μm and is associated with an UCHII region, an IRAS source,

Table 3 Information on the Sources Associated with Cloud A

Associated source name	Frequency	RA	Dec	V (km s^{-1})	Reference
(1)	(2)	(3)	(4)	(5)	(6)
UCHII G31.28+0.06		18:48:12.0	–01:26:29	109.9	Kurtz et al. (1994); Becker et al. (1994)
IRAS 18456–0129		18:48:15.1	–01:26:25	109.9	Helou & Walker (1988)
OH masers	1665 MHz, 1667 MHz	18:48:12.5	–01:26:30	103–108.5	(Caswell et al. 2013)
	1665 MHz	18:48:12.5	–01:26:30	107.2	Forster & Caswell (1989)
H_2O masers	23.235 GHz	18:48:11.9	–01:26:38	109.0	Forster & Caswell (1989)
		18:48:11.9	–01:26:38	108.3	Forster & Caswell (1999)
class II CH_3OH masers	6.7 GHz, 12.2 GHz	18:48:15.1	–01:26:25	110.4,110.6	Błaszkiewicz & Kus (2004)

Notes: If the velocity is a single value in Column (5), it represents the $V_{\rm LSR}$ of the source. Otherwise, it represents a velocity interval of the source. As for CH_3OH masers, there are two values corresponding to two frequencies.

H_2O masers, CH_3OH masers and OH masers, implying the possibility of massive star formation in this core.

– The molecular emission and dust emission both suggest that clouds A and B may be adjacent in space.
– The distribution of dust temperature shows a ~ 21 K shell, together with a colder cavity inside the shell, while the distribution of the H_2 column density presents an anti-correlation with the temperature within the shell: colder dust temperature with higher column density.
– The NVSS 1.4 GHz radio emission traces an expanding HII region in the compact core of cloud A, which shows a bulge to the northeast, indicating that the expansion rate is faster in the northeast or the surrounding medium in the northeast is more diffuse. We estimate the expansion timescale of the HII region to be $(0.03 - 0.09)$ Myr.

Acknowledgements We thank the referee for sincere advice. We are grateful to the staff at Qinghai Station of PMO for their assistance during the observations. We also thank the Key Laboratory for Radio Astronomy, CAS for partly supporting the operation of the telescope. This work is supported by the National Key Basic Research Program of China (No. 2015CB857100). This work is also supported by the National Natural Science Foundation of China (Grant Nos. 11403052, 11363004 and 11403042).

Appendix A: THE MAPPING GRIDS

Figure A.1 presents the mapping grids with $30''$ spacing in $C^{13}O$ (1–0) and $C^{18}O$ (1–0) lines, which exhibit several components towards IRDC G31.23+0.05.

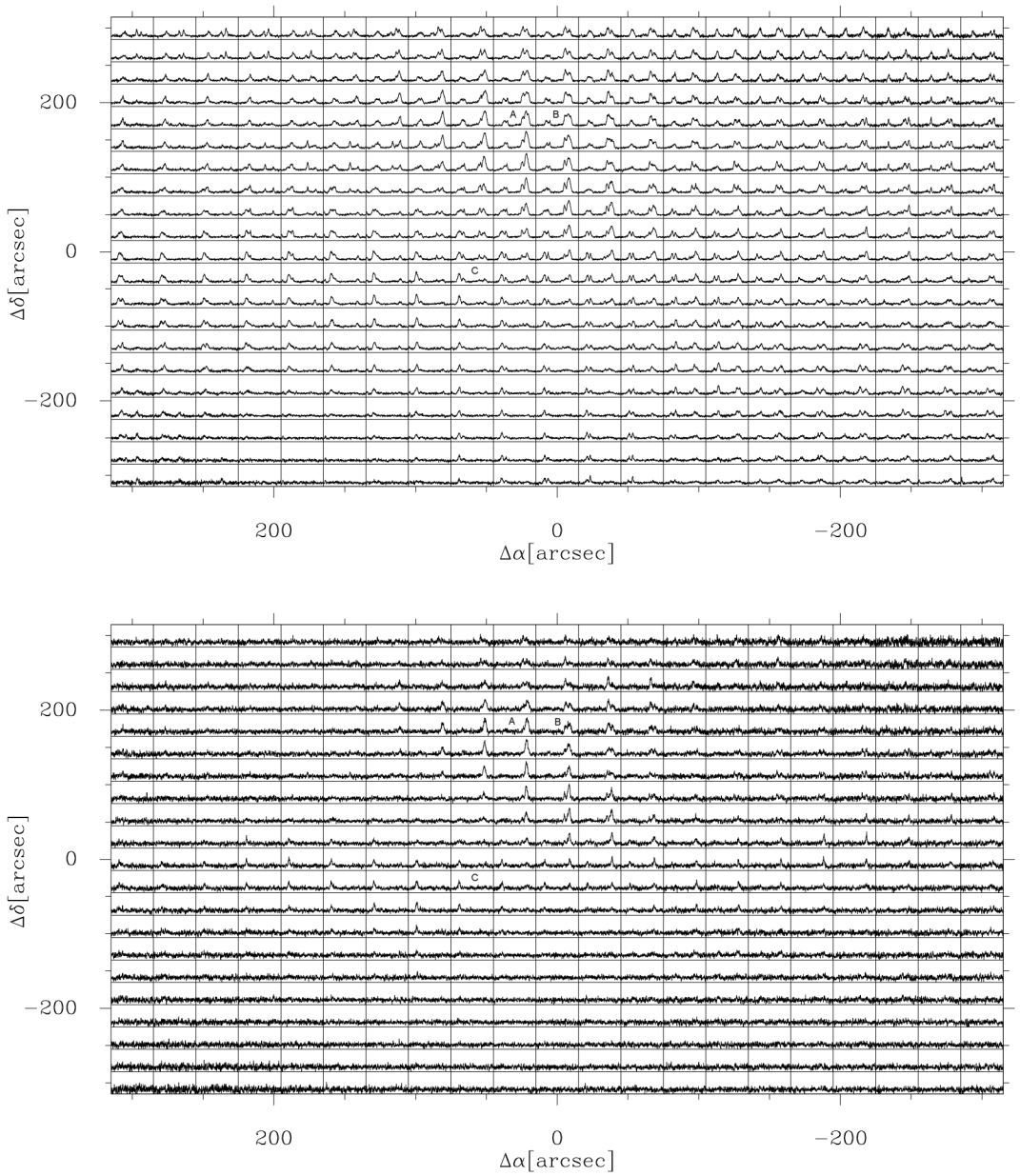

Fig. A.1 Spectral lines towards IRDC G31.23+0.05. The $C^{13}O$ (1–0) grid with $30''$ spacing is in the top panel and the $C^{18}O$ (1–0) grid with $30''$ spacing is in the bottom panel. The X- and Y-axes are the R.A. and Dec. offsets in arcseconds, respectively. Letters A, B and C in the grids mark the peak positions of three IRDCs.

References

Anderson, L. D., Zavagno, A., Deharveng, L., et al. 2012, A&A, 542, A10

Ballesteros-Paredes, J., Hartmann, L. W., Vázquez-Semadeni, E., Heitsch, F., & Zamora-Avilés, M. A. 2011, MNRAS, 411, 65

Becker, R. H., White, R. L., Helfand, D. J., & Zoonematkermani, S. 1994, ApJS, 91, 347

Beckwith, S. V. W., Sargent, A. I., Chini, R. S., & Guesten, R. 1990, AJ, 99, 924

Beuther, H., Ragan, S. E., Johnston, K., et al. 2015, A&A, 584, A67

Błaszkiewicz, L., & Kus, A. J. 2004, A&A, 413, 233

Bronfman, L., Nyman, L.-A., & May, J. 1996, A&AS, 115, 81

Busquet, G., Zhang, Q., Palau, A., et al. 2013, ApJ, 764, L26

Carey, S. J., Clark, F. O., Egan, M. P., et al. 1998, ApJ, 508, 721

Caswell, J. L., Green, J. A., & Phillips, C. J. 2013, MNRAS, 431, 1180

Chambers, E. T., Jackson, J. M., Rathborne, J. M., & Simon, R. 2009, ApJS, 181, 360
Condon, J. J., Cotton, W. D., Greisen, E. W., et al. 1998, AJ, 115, 1693
Dewangan, L. K., Ojha, D. K., Luna, A., et al. 2016, ApJ, 819, 66
Dirienzo, W. J., Brogan, C., Indebetouw, R., et al. 2015, AJ, 150, 159
Dobbs, C. L., Krumholz, M. R., Ballesteros-Paredes, J., et al. 2014, Protostars and Planets VI, 3
Duarte-Cabral, A., Dobbs, C. L., Peretto, N., & Fuller, G. A. 2011, A&A, 528, A50
Dyson, J. E., & Williams, D. A. 1980, Physics of the Interstellar Medium (New York: Halsted Press)
Egan, M. P., Shipman, R. F., Price, S. D., et al. 1998, ApJ, 494, L199
Faimali, A., Thompson, M. A., Hindson, L., et al. 2012, MNRAS, 426, 402
Forster, J. R., & Caswell, J. L. 1989, A&A, 213, 339
Forster, J. R., & Caswell, J. L. 1999, A&AS, 137, 43
Frerking, M. A., Langer, W. D., & Wilson, R. W. 1982, ApJ, 262, 590
Furukawa, N., Dawson, J. R., Ohama, A., et al. 2009, ApJ, 696, L115
Glenn, J., Aguirre, J., Bally, J., et al. 2009, in Astronomical Society of the Pacific Conference Series, 417, Submillimeter Astrophysics and Technology: a Symposium Honoring Thomas G. Phillips, eds. D. C. Lis, J. E. Vaillancourt, P. F. Goldsmith, T. A. Bell, N. Z. Scoville, & J. Zmuidzinas, 277
Griffin, M. J., Abergel, A., Abreu, A., et al. 2010, A&A, 518, L3
Haworth, T. J., Tasker, E. J., Fukui, Y., et al. 2015, MNRAS, 450, 10
Helou, G., & Walker, D. W., eds. 1988, Infrared Astronomical Satellite (IRAS) Catalogs and Atlases. The Small Scale Structure Catalog, 7, 1
Henshaw, J. D., Caselli, P., Fontani, F., et al. 2013, MNRAS, 428, 3425
Henshaw, J. D., Caselli, P., Fontani, F., Jiménez-Serra, I., & Tan, J. C. 2014, MNRAS, 440, 2860
Higuchi, A. E., Chibueze, J. O., Habe, A., Takahira, K., & Takano, S. 2014, AJ, 147, 141
Jackson, J. M., Rathborne, J. M., Shah, R. Y., et al. 2006, ApJS, 163, 145
Jiménez-Serra, I., Caselli, P., Tan, J. C., et al. 2010, MNRAS, 406, 187
Jiménez-Serra, I., Caselli, P., Fontani, F., et al. 2014, MNRAS, 439, 1996
Kauffmann, J., Bertoldi, F., Bourke, T. L., Evans, II, N. J., & Lee, C. W. 2008, A&A, 487, 993
Kurtz, S., Churchwell, E., & Wood, D. O. S. 1994, ApJS, 91, 659
Liu, X.-L., Wang, J.-J., & Xu, J.-L. 2013, MNRAS, 431, 27
Liu, X.-L., Wang, J.-J., & Xu, J.-L. 2014, MNRAS, 443, 2264
Longmore, S. N., Burton, M. G., Barnes, P. J., et al. 2007, MNRAS, 379, 535
Markwardt, C. B. 2009, in Astronomical Society of the Pacific Conference Series, 411, Astronomical Data Analysis Software and Systems XVIII, eds. D. A. Bohlender, D. Durand, & P. Dowler, 251
Mateen, M., Hofner, P., & Araya, E. 2006, ApJS, 167, 239
Myers, P. C., Linke, R. A., & Benson, P. J. 1983, ApJ, 264, 517
Parsons, H., Thompson, M. A., & Chrysostomou, A. 2009, MNRAS, 399, 1506
Perault, M., Omont, A., Simon, G., et al. 1996, A&A, 315, L165
Peretto, N., Fuller, G. A., André, P., et al. 2014, A&A, 561, A83
Pitann, J., Linz, H., Ragan, S., et al. 2013, ApJ, 766, 68
Poglitsch, A., Waelkens, C., Geis, N., et al. 2010, A&A, 518, L2
Pomarès, M., Zavagno, A., Deharveng, L., et al. 2009, A&A, 494, 987
Pon, A., Johnstone, D., Caselli, P., et al. 2016, A&A, 587, A96
Rathborne, J. M., Jackson, J. M., & Simon, R. 2006, ApJ, 641, 389
Reid, M. J., Menten, K. M., Zheng, X. W., et al. 2009, ApJ, 700, 137
Sanhueza, P., Jackson, J. M., Foster, J. B., et al. 2013, ApJ, 773, 123
Schuller, F., Menten, K. M., Contreras, Y., et al. 2009, A&A, 504, 415
Scoville, N. Z., Sargent, A. I., Sanders, D. B., et al. 1986, ApJ, 303, 416
Sun, N., & Wu, Y. 2013, New Astron., 22, 1
Szymczak, M., Hrynek, G., & Kus, A. J. 2000, A&AS, 143, 269
Szymczak, M., & Gérard, E. 2004, A&A, 414, 235
Vallee, J. P. 1995, AJ, 110, 2256
Vázquez-Semadeni, E., Gómez, G. C., Jappsen, A.-K., Ballesteros-Paredes, J., & Klessen, R. S. 2009, ApJ, 707, 1023
Watson, C., Povich, M. S., Churchwell, E. B., et al. 2008, ApJ, 681, 1341
Zhang, B., Moscadelli, L., Sato, M., et al. 2014, ApJ, 781, 89
Zhang, C.-P., Li, G.-X., Wyrowski, F., et al. 2016, A&A, 585, A117